

Topological Magnonic Properties of an Antiferromagnetic Chain

Topojit Debnath,^{1,*} Shri Hari Soundararaj,^{2,†} Sohee Kwon,^{1,‡} Alexander A. Balandin,^{3,§} and Roger K. Lake^{1,¶}

¹*Laboratory for Terahertz & Terascale Electronics (LATTE),*

*Department of Electrical and Computer Engineering,
University of California, Riverside, CA, 92521, USA*

²*Materials Science and Engineering, University of California, Riverside, CA, 92521, USA*

³*Department of Materials Science and Engineering,
University of California, Los Angeles, CA 90095, USA*

(Dated: October 15, 2024)

The magnonic excitations of a dimerized, one-dimensional, antiferromagnetic chain can be trivial or topological depending on the signs and magnitudes of the alternating exchange couplings and the anisotropy. The topological phase that occurs when the signs of the two different exchange couplings alternate is qualitatively different from that of the Su-Schrieffer-Heeger model. A material that may exhibit these properties is the quasi-one-dimensional material MoI_3 that consists of dimerized chains weakly coupled to adjacent chains. The magnetic ground state and its excitations are analyzed both analytically and numerically using exchange and anisotropy parameters extracted from density functional theory calculations.

I. INTRODUCTION

Anti-ferromagnetism and topological magnonics [1–4] in low-dimensional materials are of high current interest. The majority of the work in topological magnonics has focused on two-dimensional (2D) ferromagnetic (FM) and antiferromagnetic (AFM) systems. The 2D systems generally rely on the presence of the Dzyaloshinskii-Moriya interaction, which serves as an analogue to spin-orbit coupling in electronic systems, to obtain a topological magnonic phase. In one-dimensional electronic systems, dimerization can result in a topological phase described by the Su-Schrieffer-Heeger (SSH) model [5], and in one-dimensional FM systems, dimerization results in a magnetic analogue of the SSH model with a topological magnonic phase [6, 7]. We will show that dimerization alone does not qualitatively alter the magnonic spectrum in an AFM spin chain, and that more is required to obtain a topological magnonic phase.

In this paper, we analyze the magnonic properties of a AFM dimerized and tetramerized spin chain. Dimerization causes the AFM exchange coupling between the magnetic atoms along the chain to alternate in magnitude. The two different intrachain exchange couplings, J_1 and J_2 , are illustrated in Fig. 1(d). With $J_1 > J_2 > 0$ (AFM coupling) the magnonic spectrum remains trivial for all positive values of J_1 and J_2 . If J_2 becomes negative, such that the sign of the exchange coupling along the chain alternates, then, depending on the relative magnitudes of J_1 , J_2 , and the anisotropy constants, the magnonic spectrum can enter a non-trivial topological state that is qualitatively different from that of the

SSH model.

An example quasi-one-dimensional material that may exhibit these magnonic topological properties is the quasi-one-dimensional transition metal tri-halide MoI_3 . It consists of covalently bonded MoI_3 chains weakly coupled to adjacent chains in a triangular lattice. The material was recently synthesized and characterized with powder and single-crystal X-ray analysis [8–10]. The crystal system is orthorhombic with space group $Pmnm$ (59). The chains are dimerized with alternating distances, 2.88 Å and 3.53 Å, between Mo atoms along the chains. There is no known temperature for the chains to transition to the symmetric phase ($P6_3/mmc$). Each Mo atom is bonded to 6 I atoms in a distorted octahedral arrangement. A bulk unit cell, doubled along the b axis, is shown from top and side views in Fig. 1(a,b). Bulk samples were characterized by Raman spectroscopy [10]. The temperature variation of several Raman peaks displayed a transition suggestive of a magnetic phase transition. Several peaks that disappeared in the temperature range between 125 - 150 K were considered to originate from two magnon scattering processes. Density functional theory (DFT) calculations found that the lowest energy ground state was easy-plane AFM with alternating spins along the chains. Prior DFT calculations of single chains of transition metal di- and tri-halides also found the ground state of MoI_3 to be AFM [11, 12].

Exchange coupling constants and anisotropy energies determined from DFT calculations in Sec. II are used in a Heisenberg type Hamiltonian that is analyzed using linear spin wave theory [15–17] in the main text and classical effective field theory in the Appendix. Analytical expressions are derived in Sec. III for an individual chain that explicitly show the criteria for transitioning from a topologically trivial to a non-trivial phase. The full magnonic spectrum that includes the interchain coupling is determined numerically in Sec. IV.

* tdebn001@ucr.edu

† ssoun005@ucr.edu

‡ skwon054@ucr.edu

§ balandin@seas.ucla.edu

¶ Corresponding author: rlake@ucr.edu

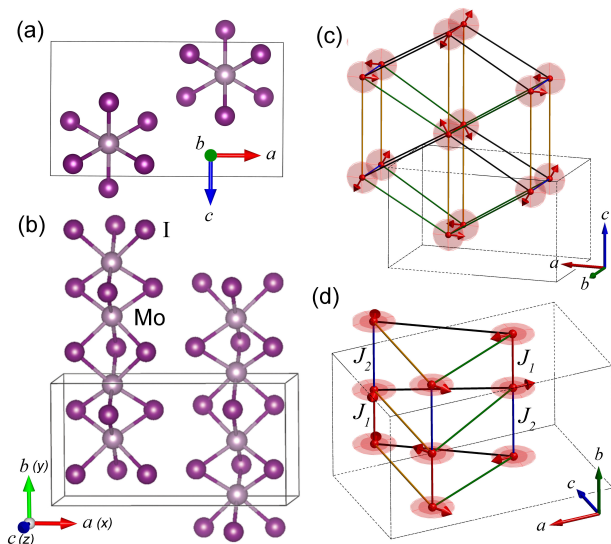


FIG. 1. (a) Top view and (b) side view of two chains that comprise the MoI_3 unit cell. The chains have been doubled along the b axis to show the dimerization. The lattice vector directions, xyz coordinate system, and outline of the unit cell are shown. (c) Relaxed magnetic structure showing only the Mo atoms of a central chain and its six surrounding chains. The circular regions around each spin indicate easy plane anisotropy perpendicular to the axis of the chains. (d) Relaxed magnetic structure illustrating the exchange coupling parameters. Figures are generated by (a,b) Vesta [13] and (c,d) SpinW [14].

II. DENSITY FUNCTIONAL THEORY CALCULATIONS

Density functional theory calculations, as implemented in the Vienna *ab initio* simulation package (VASP) [18–21], are performed using the generalized gradient approximation for the exchange-correlation functional as parameterized by Perdew, Burke, and Ernzerhof (PBE) [22]. The van der Waals interaction is included using the PBE-D3 method of Grimme *et al.* [23]. The energy cutoff for the plane wave basis is 520 eV. Bulk structures are relaxed until the forces on the atoms are smaller than 10^{-4} eV/Å. Phonon calculations are performed using the finite-displacement supercell approach as implemented in Phonopy [24, 25] with a $2 \times 2 \times 2$ supercell, and the Brillouin zone is sampled by a $3 \times 6 \times 6$ Monkhorst–Pack k-point grid.

Previously, a Hubbard U value of 4 eV was used to prevent the occurrence of negative phonon modes in the phonon dispersion calculations [10]. In this work, we find that by using a tighter convergence criteria during the structure relaxation process, a stable crystal structure can be obtained without including a Hubbard U term. The self consistent field electronic calculations with $U = 0$, $U = 2.4$ eV [26], and $U = 4$ eV [10] all show the easy-plane AFM spin configuration, with alternating spins along the chains, to be the minimum energy mag-

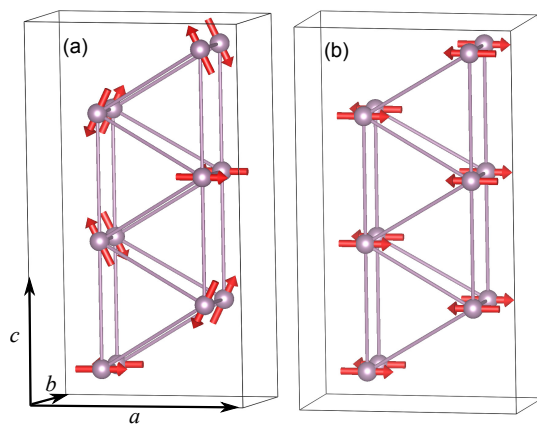


FIG. 2. Magnetic configurations of the MoI_3 $1 \times 1 \times 3$ supercell for the (a) non-collinear antiferromagnet state and (b) collinear antiferromagnet. Only the Mo atoms are shown.

netic ground state. However, when the crystal structure is relaxed in the AFM phase, only the $U = 0$ calculation results in the dimerized $Pm\bar{m}n$ ground state. The $U \neq 0$ calculations find the non-dimerized $Pm\bar{m}n$ phase to be the ground state, which contradicts the experimental results. The total energy difference per unit cell of the dimerized and non-dimerized $Pm\bar{m}n$ phase (calculated with $U = 0$ in the AFM phase) is 0.43 eV. Furthermore, the $U = 0$ calculation gives lattice constants ($a = 12.41$ Å, $b = 6.45$ Å, and $c = 7.17$ Å) that agree closely with the experimental values [10]. Therefore, all calculations in this work are performed without a Hubbard U correction.

To investigate the inter-chain spin alignment of the charge neutral ground state, we constructed a $1 \times 1 \times 3$ supercell and compared the total energies of the non-collinear and collinear AFM states, as shown in Fig. 2. In the collinear configuration, the magnetic moments are aligned along the $\pm a$ axis. In the non-collinear configuration, the magnetic moments of the Mo atoms in the same plane that form the vertices of a triangle are rotated with respect to each other by 120° as shown in Fig. 2(a). The DFT calculations reveal that the non-collinear AFM state is energetically favored by 14.5 meV compared to the collinear AFM state. This is also the minimum energy state found from the Heisenberg Hamiltonian (1) using exchange parameters extracted from the DFT calculations.

The the magnetic exchange coupling constants and anisotropy energies are determined from the standard energy mapping method [10, 27–29] with total energies calculated using PBE-D3 with spin-orbit coupling (SOC). The details of the these calculations and an illustration of the interchain exchange parameters, J_3 and J_4 , are provided in Appendix A. The results are shown in Table I. In the charge neutral state, all of the exchange coupling parameters are positive (AFM), and the minimum energy spin configuration along the chain, determined from DFT, is illustrated in Fig. 3(a). With $A_y = 2.11$ meV

Filling	Neutral	0.1	0.19	0.196	0.2	0.3	0.4
J_1	24.08	23.80	23.86	23.88	23.89	24.39	25.42
J_2	4.44	2.04	0.02	-0.11	-0.20	-2.30	-4.26
J_3	0.55	0.61	0.67	0.68	0.68	0.74	0.82
J_4	0.12	0.16	0.19	0.19	0.19	0.21	0.21
A_y	2.11	2.38	2.57	2.58	2.58	2.76	2.90
A_x	0	0.12	0.33	0.35	0.36	0.62	0.91

TABLE I. Exchange and anisotropy parameters (meV) as a function of hole filling (number of excess holes per unit cell consisting of 4 Mo atoms and 12 I atoms).

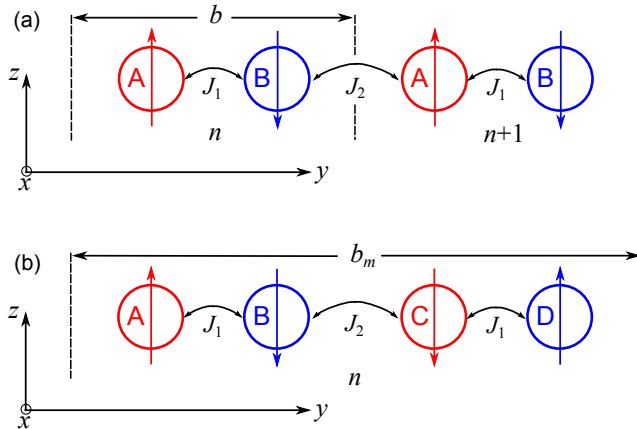


FIG. 3. (a) Dimerized AFM chain with $J_1, J_2 > 0$. There are 2 Mo atoms per unit cell labeled as A and B. The unit cell indices shown are n and $n + 1$. The lattice constant is b for both the crystal lattice and the magnetic lattice. The coordinate system corresponding to the crystallographic axes is also shown. The chain lies along the y direction. The spins lie in the x - z plane perpendicular to the chain axis. We assume an arbitrarily small in-plane anisotropy and align the equilibrium spins along the z -axis. (b) Magnetic unit cell with $J_1 > 0$ and $J_2 < 0$. The coupling now alternates between AFM and FM. The magnetic unit cell length $b_m = 2b$ doubles so that there are 4 Mo atoms in the magnetic unit cell labelled A - D. We refer to this as the magnetically tetramerized unit cell.

and $A_x = 0$, the spins have easy-plane anisotropy with the easy-plane perpendicular to the chains, as illustrated in Fig. 1(c,d). With hole filling, J_2 changes sign and the minimum energy spin configuration along the chain switches to that shown in Fig. 3(b). We will refer to this as the magnetically tetramerized unit cell. Furthermore, the in-plane anisotropy A_x increases, so that at larger values of hole filling, the ground state spin configuration becomes collinear with all spins aligned along $\pm \mathbf{c}$. We analyze the excitations of the magnetic system by first considering the individual chains and then consider the effect of interchain coupling.

III. SINGLE CHAIN ANALYSIS

A. Dimerized AFM Single Chain

We begin by analyzing a single chain illustrated in Fig. 3(a) using parameters for the charge neutral state given in Table I. We do this because the bulk crystal is physically a lattice of weakly coupled chains, and the characteristics of the single chain are still present and visible when interchain coupling is included. Furthermore, the single chain provides a model system to compare against other such model systems found in the literature, falling under the general umbrella of the SSH model. The spin Hamiltonian for this system is

$$\begin{aligned}
 H = & 2 \sum_n [J_1 \mathbf{S}_n^A \cdot \mathbf{S}_n^B + J_2 \mathbf{S}_n^A \cdot \mathbf{S}_{n-1}^B] \\
 & + A_y \sum_n [(\mathbf{S}_{n,y}^A)^2 + (\mathbf{S}_{n,y}^B)^2] \\
 & + A_x \sum_n [(\mathbf{S}_{n,x}^A)^2 + (\mathbf{S}_{n,x}^B)^2].
 \end{aligned} \tag{1}$$

In Eq. (1), $J_1, J_2 > 0$, i.e. both exchange couplings are antiferromagnetic, and $J_1 > J_2$. J_1 is the exchange coupling between the A and B spins within the same unit cell, and J_2 couples spins between adjacent unit cells. The sum is over unit cells n . $A_y \gg A_x > 0$ are anisotropy terms. A_y creates easy-plane anisotropy with the easy plane in the x - z plane perpendicular the axis of the chain. Within the x - z plane a small anisotropy A_x is assumed such that the equilibrium spins minimize their energy by aligning and anti-aligning along z .

The magnon excitation spectrum can be calculated using the classical effective field approach or the quantum approach and linear spin wave theory [15–17]. Here, we will use the quantum approach and linear spin wave theory, and, in Appendix D, we describe the effective field approach. Both approaches result in the same magnon dispersion, however the quantum approach allows for the calculation of the surface Green's function using the standard decimation algorithm [30–32].

The analysis begins with the Holstein-Primakoff transformation [33] of the spin operators in Eq. (1). To lowest order in the spin deviation operators,

$$\begin{aligned}
 \hat{S}_{j,z}^A &= S - \hat{n}_j^A \\
 \hat{S}_j^{A+} &\approx \sqrt{2S} a_j \\
 \hat{S}_j^{A-} &\approx \sqrt{2S} a_j^\dagger
 \end{aligned} \tag{2}$$

and

$$\begin{aligned}
 \hat{S}_{j,z}^B &= -S + \hat{n}_j^B \\
 \hat{S}_j^{B+} &\approx \sqrt{2S} b_j^\dagger \\
 \hat{S}_j^{B-} &\approx \sqrt{2S} b_j
 \end{aligned} \tag{3}$$

where $\hat{n}_j^A = a_j^\dagger a_j$, $\hat{n}_j^B = b_j^\dagger b_j$ and $n_j \in \{0, 1, 2, \dots, 2S\}$ so that $S_{j,z}^A$ and $S_{j,z}^B$ run from $-S$ to S . The creation and

annihilation operators follow the usual bosonic commutation relations. Making the above substitutions into Eq.

(1), using $S_x = \frac{1}{2}(S^+ + S^-)$ and $S_y = \frac{1}{2i}(S^+ - S^-)$, and keeping terms up to quadratic order, we have, $H \equiv H_{J_1} + H_{J_2} + H_A$ where

$$H_{J_1} = 2J_1S \left\{ -NS + \sum_n (a_n b_n + a_n^\dagger b_n^\dagger + a_n^\dagger a_n + b_n^\dagger b_n) \right\} \quad (4)$$

$$H_{J_2} = 2J_2S \left\{ -NS + \sum_n (a_n b_{n-1} + a_n^\dagger b_{n-1}^\dagger + a_n^\dagger a_n + b_{n-1}^\dagger b_{n-1}) \right\} \quad (5)$$

$$H_A = -\frac{A_y - A_x}{2}S \sum_n (a_n a_n + a_n^\dagger a_n^\dagger + b_n b_n + b_n^\dagger b_n^\dagger) + \frac{A_y + A_x}{2} \sum_n (a_n a_n^\dagger + a_n^\dagger a_n + b_n^\dagger b_n + b_n b_n^\dagger). \quad (6)$$

Defining the Fourier transforms as $a_n = \frac{1}{\sqrt{N}} \sum_q e^{iqbn} a_q$, and $b_n = \frac{1}{\sqrt{N}} \sum_q e^{iqbn} b_q$, where b is the lattice constant of the 1D chain shown in Fig. 3(a), n is the unit cell index, and $q \in \{-\pi/b, \pi/b\}$, the transformed Eqs. (4)-(6) become

$$\begin{aligned} H_{J_1} &= 2J_1S \left\{ -NS + \sum_q (a_{-q} b_q + a_q^\dagger b_{-q}^\dagger + a_q^\dagger a_q + b_q^\dagger b_q) \right\} \\ H_{J_2} &= 2J_2S \left\{ -NS + \sum_q (e^{iqb} a_q b_{-q} + e^{-iqb} a_q^\dagger b_{-q}^\dagger + a_q^\dagger a_q + b_q^\dagger b_q) \right\} \\ H_A &= -\frac{A_y - A_x}{2}S \sum_q (a_q a_{-q} + a_q^\dagger a_{-q}^\dagger + b_q b_{-q} + b_q^\dagger b_{-q}^\dagger) + \frac{A_y + A_x}{2}S \sum_q (a_q a_q^\dagger + a_q^\dagger a_q + b_q^\dagger b_q + b_q b_q^\dagger). \end{aligned} \quad (7)$$

There is considerable flexibility in the way we write Eq. (7), since for any term, we can let $q \rightarrow -q$, and we can also apply the commutation relations to re-arrange any pair of operators. We use this flexibility to arrange the Hamiltonian into a manifestly Hermitian form.

$$\begin{aligned} H &= -4S(J_1 + J_2)NS \\ &+ S \sum_q \left[(J_1 + J_2 e^{iqb}) (b_{-q} a_q + b_q^\dagger a_{-q}^\dagger) + (J_1 + J_2 e^{-iqb}) (a_q^\dagger b_{-q}^\dagger + a_{-q} b_q) \right] \\ &+ S \sum_q \left[\left(J_1 + J_2 + \frac{A_y + A_x}{2} \right) (a_q^\dagger a_q + a_{-q} a_{-q}^\dagger + b_q^\dagger b_q + b_{-q} b_{-q}^\dagger) \right] - \frac{A_y - A_x}{2}S \sum_q (a_{-q} a_q + a_q^\dagger a_{-q}^\dagger + b_{-q} b_q + b_q^\dagger b_{-q}^\dagger) \end{aligned} \quad (8)$$

We now follow an approach described by White *et al.* [34] and Colpa [35], which is a common approach for calculating magnon energies in AFMs [4, 14, 17]. Ignoring the constant term, we write H as

$$H = \frac{1}{2} \sum_q \mathbf{X}^\dagger(q) \mathbf{H}(q) \mathbf{X}(q) \quad (9)$$

where \mathbf{X} is a column vector of 4 operators, and \mathbf{H} is a 4×4 matrix of c -numbers. We choose $\mathbf{X} = [a_q \ b_q \ a_{-q}^\dagger \ b_{-q}^\dagger]^T$. \mathbf{X} satisfies the matrix commutation relation $[\mathbf{X}, \mathbf{X}^\dagger] \equiv \mathbf{X}(\mathbf{X}^*)^T - (\mathbf{X}^* \mathbf{X}^T)^T \equiv \mathbf{g}_a = \sigma_z \otimes \mathbf{I}$ where σ_z is the Pauli matrix, \mathbf{I} is the 2×2 identity matrix, \mathbf{X}^* is the column vector \mathbf{X} with the operators daggered, and $(\mathbf{X}^*)^T = \mathbf{X}^\dagger$. The matrix $\mathbf{H}(q)$ is

$$\mathbf{H}(q) = 2S \begin{bmatrix} \Sigma & 0 & -\Delta_A & (J_1 + J_2 e^{-iqb}) \\ 0 & \Sigma & (J_1 + J_2 e^{iqb}) & -\Delta_A \\ -\Delta_A & (J_1 + J_2 e^{-iqb}) & \Sigma & 0 \\ (J_1 + J_2 e^{iqb}) & -\Delta_A & 0 & \Sigma \end{bmatrix} \quad (10)$$

where $\Sigma = \left(J_1 + |J_2| + \frac{A_y + A_x}{2} \right)$ and $\Delta_A = \frac{A_y - A_x}{2}$.

The eigenenergies of the excitations are determined from the generalized eigenvalue equation $|\mathbf{H}(q) - \mathbf{g}_a \hbar \omega| = 0$. Since \mathbf{g}_a is invertible, and $\mathbf{g}_a^{-1} = \mathbf{g}_a$, this is also easily converted into a regular eigenvalue equation, $|\mathbf{H}(q) \mathbf{g}_a - \mathbf{I} \hbar \omega| = 0$

where \mathbf{I} is the identity matrix. There are 4 solutions of the form $\pm\hbar\omega_0$ and $\pm\hbar\omega_1$. The two positive solutions give the $\omega - k$ relations of the two magnon modes. The dispersion relations for the two positive energy modes are

$$\hbar\omega_0(k) = 2S \left[4J_1J_2 \sin^2\left(\frac{kb}{2}\right) - (A_y - A_x)(J_1 + J_2) \sqrt{1 - \frac{4J_1J_2 \sin^2\left(\frac{kb}{2}\right)}{(J_1 + J_2)^2}} + (A_y + A_x)(J_1 + J_2) + A_yA_x \right]^{1/2} \quad (11)$$

and

$$\hbar\omega_1(k) = 2S \left[4J_1J_2 \sin^2\left(\frac{kb}{2}\right) + (A_y - A_x)(J_1 + J_2) \sqrt{1 - \frac{4J_1J_2 \sin^2\left(\frac{kb}{2}\right)}{(J_1 + J_2)^2}} + (A_y + A_x)(J_1 + J_2) + A_yA_x \right]^{1/2}. \quad (12)$$

The dispersion of the single dimerized AFM chain, calculated from Eqs. (11) and (12), is plotted in Fig. 4(a) using parameters from Table I for the charge neutral structure. To show the effect of in-plane anisotropy, a value of $A_x = 0.002$ meV $\approx A_y/1000$ is also used. In the absence of anisotropy ($A_y = A_x = 0$), the dispersions of both modes reduce to the standard dispersion of a 1D AFM chain [36] with the uniform exchange coupling replaced by the geometric mean of the two different exchange couplings,

$$\hbar\omega_0(k) = 4S\sqrt{J_1J_2} \sin\left(\frac{kb}{2}\right). \quad (13)$$

Unlike the ferromagnetic chain, in which dimerization gaps the magnon spectrum in the middle of the band in analogy with the Su-Schrieffer-Heeger (SSH) model for electrons [6], the dimerization of an AFM chain does not qualitatively alter the spectrum. It remains linear and gapless.

The energies at Γ are

$$\hbar\omega_0 = 2S\sqrt{2A_x(J_1 + J_2 + A_y/2)} \approx 2S\sqrt{2A_x(J_1 + J_2)} \quad (14)$$

and

$$\hbar\omega_1 = 2S\sqrt{2A_y(J_1 + J_2 + A_x/2)} \approx 2S\sqrt{2A_y(J_1 + J_2)}. \quad (15)$$

Thus, even though the in-plane anisotropy A_x may be extremely small, the fundamental gap $\hbar\omega_0$ in the spectrum is determined by the geometric mean of the in-plane anisotropy and the exchange coupling, and this can be 2 orders of magnitude larger than the small anisotropy energy.

At the zone boundary ($k = \pi/b$), the energies are

$$\hbar\omega_0(\pi/b) = 4S\sqrt{J_1J_2} \left[1 + \frac{A_yJ_2 + A_xJ_1 + A_yA_x/2}{2J_1J_2} \right]^{1/2} \quad (16)$$

$$\hbar\omega_1(\pi/b) = 4S\sqrt{J_1J_2} \left[1 + \frac{A_yJ_1 + A_xJ_2 + A_yA_x/2}{2J_1J_2} \right]^{1/2} \quad (17)$$

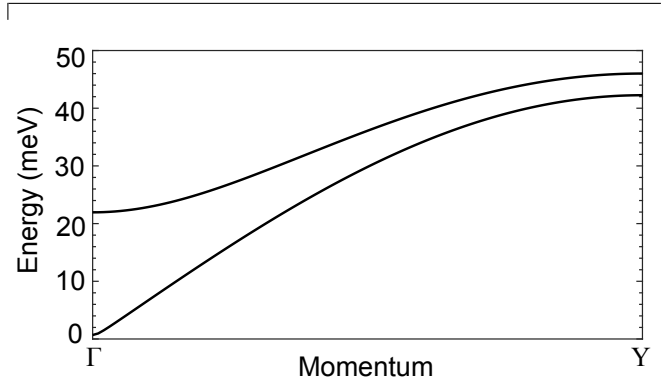


FIG. 4. Magnon spectrum of a single 1D dimerized AFM chain calculated from Eqs. (11) and (12). The values of J_1 , J_2 , and A_y are from the ‘Neutral’ column of Table I. In addition, A_x is set to $2 \mu\text{eV}$ to show the effect of small in-plane anisotropy.

Expanding out the square root to first order,

$$\hbar\omega_0(\pi/b) \approx 4S\sqrt{J_1J_2} \left\{ 1 + \frac{A_yJ_2 + A_xJ_1 + A_yA_x/2}{4J_1J_2} \right\} \quad (18)$$

$$\hbar\omega_1(\pi/b) \approx 4S\sqrt{J_1J_2} \left\{ 1 + \frac{A_yJ_1 + A_xJ_2 + A_yA_x/2}{4J_1J_2} \right\}, \quad (19)$$

and taking the difference of the above two equations gives

$$\hbar\omega_1(\pi/b) - \hbar\omega_0(\pi/b) = \frac{S(J_1 - J_2)(A_y - A_x)}{\sqrt{J_1J_2}}. \quad (20)$$

From Eq. (20), we see that splitting of the two modes at the zone edge requires both dimerization ($J_1 \neq J_2$) and anisotropy.

B. Tetramerized AFM-FM Single Chain

When J_2 changes sign, the magnetic ground state of the single chain becomes that shown in Fig. 3(b). The spin Hamiltonian retains the same form as Eq. (1), except now, $J_1 > 0$, $J_2 < 0$, and there are 4 atoms in the

magnetic unit cell. The Hamiltonian is now

$$H = 2 \sum_n \left[J_1 \mathbf{S}_n^A \cdot \mathbf{S}_n^B + J_2 \mathbf{S}_n^B \cdot \mathbf{S}_n^C + J_1 \mathbf{S}_n^C \cdot \mathbf{S}_n^D + J_2 \mathbf{S}_n^D \cdot \mathbf{S}_{n+1}^A \right] + A_y \sum_{n,\alpha} (\mathbf{S}_{n,y}^\alpha)^2 + A_x \sum_{n,\alpha} (\mathbf{S}_{n,x}^\alpha)^2, \quad (21)$$

where α is the atom index $\{A, B, C, D\}$. The Holstein-Primakoff transformations for the spin operators \mathbf{S}^A and

\mathbf{S}^B remain the same as given by Eqs. (2) and (3). The Holstein-Primakoff transformations for \mathbf{S}^C and \mathbf{S}^D are

$$\begin{aligned} \hat{S}_{j,z}^C &= -S + \hat{n}_j^C; \quad \hat{S}_j^{C+} \approx \sqrt{2S} c_j^\dagger; \quad \hat{S}_j^{C-} \approx \sqrt{2S} c_j \\ \hat{S}_{j,z}^D &= S - \hat{n}_j^D; \quad \hat{S}_j^{D+} \approx \sqrt{2S} d_j; \quad \hat{S}_j^{D-} \approx \sqrt{2S} d_j^\dagger \end{aligned} \quad (22)$$

Writing out H in Eq. (21) as the parts proportional to J_1 , J_2 , and the anisotropy terms gives

$$\begin{aligned} H_{J_1} &= 2J_1 S \left\{ -2NS + \sum_n (a_n b_n + a_n^\dagger b_n^\dagger + a_n^\dagger a_n + b_n^\dagger b_n + c_n^\dagger d_n^\dagger + c_n d_n + c_n^\dagger c_n + d_n^\dagger d_n) \right\} \\ H_{J_2} &= 2|J_2| S \left\{ -2NS + \sum_n (-b_n^\dagger c_n - b_n c_n^\dagger + b_n^\dagger b_n + c_n^\dagger c_n - d_n a_{n+1}^\dagger - d_n^\dagger a_{n+1} + a_{n+1}^\dagger a_{n+1} + d_n^\dagger d_n) \right\} \\ H_A &= -\frac{A_y - A_x}{2} S \sum_n (a_n a_n + a_n^\dagger a_n^\dagger + b_n b_n + b_n^\dagger b_n^\dagger + c_n c_n + c_n^\dagger c_n^\dagger + d_n d_n + d_n^\dagger d_n^\dagger) \\ &\quad + \frac{A_y + A_x}{2} S \sum_n (a_n a_n^\dagger + a_n^\dagger a_n + b_n^\dagger b_n + b_n b_n^\dagger + c_n c_n^\dagger + c_n^\dagger c_n + d_n^\dagger d_n + d_n d_n^\dagger). \end{aligned} \quad (23)$$

Fourier transforming, we have

$$\begin{aligned} H &= 2J_1 S \left\{ -2NS + \sum_q (a_q b_{-q} + a_q^\dagger b_{-q}^\dagger + c_q d_{-q} + c_q^\dagger d_{-q}^\dagger + a_q^\dagger a_q + b_q^\dagger b_q + c_q^\dagger c_q + d_q^\dagger d_q) \right\} \\ &\quad + 2|J_2| S \left\{ -2NS + \sum_q (-b_q^\dagger c_q - b_q c_q^\dagger - e^{-iqa} d_q a_q^\dagger - e^{iqa} d_q^\dagger a_q + a_q^\dagger a_q + b_q^\dagger b_q + c_q^\dagger c_q + d_q^\dagger d_q) \right\} \\ &\quad - \frac{A_y - A_x}{2} S \sum_q (a_q a_{-q} + a_q^\dagger a_{-q}^\dagger + b_q b_{-q} + b_q^\dagger b_{-q}^\dagger + c_q c_{-q} + c_q^\dagger c_{-q}^\dagger + d_q d_{-q} + d_q^\dagger d_{-q}^\dagger) \\ &\quad + \frac{A_y + A_x}{2} S \sum_q (a_q a_q^\dagger + a_q^\dagger a_q + b_q^\dagger b_q + b_q b_q^\dagger + c_q c_q^\dagger + c_q^\dagger c_q + d_q^\dagger d_q + d_q d_q^\dagger). \end{aligned} \quad (24)$$

We again symmetrize terms to make the Hamiltonian manifestly Hermitian.

$$\begin{aligned} H &= -4NS^2 (J_1 + |J_2|) \\ &\quad + S \left(J_1 + |J_2| + \frac{A_y + A_x}{2} \right) \sum_q (a_q^\dagger a_q + a_{-q} a_{-q}^\dagger + b_q^\dagger b_q + b_{-q} b_{-q}^\dagger + c_q^\dagger c_q + c_{-q} c_{-q}^\dagger + d_q^\dagger d_q + d_{-q} d_{-q}^\dagger) \\ &\quad + J_1 S \sum_q (a_{-q} b_q + b_{-q} a_q + a_q^\dagger b_{-q}^\dagger + b_q^\dagger a_{-q}^\dagger + c_{-q} d_q + d_{-q} c_q + c_q^\dagger d_{-q}^\dagger + d_q^\dagger c_{-q}^\dagger) \\ &\quad + |J_2| S \sum_q (-b_q^\dagger c_q - c_{-q} b_{-q}^\dagger - b_{-q} c_{-q}^\dagger - c_q^\dagger b_q - e^{iqa} d_{-q} a_{-q}^\dagger - e^{-iqa} a_{-q}^\dagger d_{-q} - e^{iqa} d_q^\dagger a_q - e^{-iqa} a_q d_q^\dagger) \\ &\quad + -\frac{A_y - A_x}{2} S \sum_q (a_{-q} a_q + a_q^\dagger a_{-q}^\dagger + b_{-q} b_q + b_q^\dagger b_{-q}^\dagger + c_{-q} c_q + c_q^\dagger c_{-q}^\dagger + d_{-q} d_q + d_q^\dagger d_{-q}^\dagger) \end{aligned} \quad (25)$$

We now write H in the form of Eq. (9) with $\mathbf{X}' = [a_q \ a_{-q}^\dagger \ b_q \ b_{-q}^\dagger \ c_q \ c_{-q}^\dagger \ d_q \ d_{-q}^\dagger]^T$. We choose this ordering in preparation for the calculation of the surface Green's function, since it places the inter-unit-cell cou-

pling at the upper left and lower right diagonal blocks in the lattice representation. \mathbf{X}' satisfies commutation relation $[\mathbf{X}', \mathbf{X}'^\dagger] = \mathbf{g}_b$, where $\mathbf{g}_b = \mathbf{I} \otimes \sigma_z$, \mathbf{I} is the 4×4 identity matrix, and σ_z is the Pauli matrix. Hamiltonian (25) results in the following matrix $\mathbf{H}(q)$,

$$\mathbf{H}(q) = 2S \begin{bmatrix} \Sigma & -\Delta_A & 0 & J_1 & 0 & 0 & -|J_2|e^{-iqb_m} & 0 \\ -\Delta_A & \Sigma & J_1 & 0 & 0 & 0 & 0 & -|J_2|e^{-iqb_m} \\ 0 & J_1 & \Sigma & -\Delta_A & -|J_2| & 0 & 0 & 0 \\ J_1 & 0 & -\Delta_A & \Sigma & 0 & -|J_2| & 0 & 0 \\ 0 & 0 & -|J_2| & 0 & \Sigma & -\Delta_A & 0 & J_1 \\ 0 & 0 & 0 & -|J_2| & -\Delta_A & \Sigma & J_1 & 0 \\ -|J_2|e^{+iqb_m} & 0 & 0 & 0 & 0 & J_1 & \Sigma & -\Delta_A \\ 0 & -|J_2|e^{+iqb_m} & 0 & 0 & J_1 & 0 & -\Delta_A & \Sigma \end{bmatrix} \quad (26)$$

The eigenenergies, found from $|\mathbf{H}(q) - \mathbf{g}_b \hbar \omega| = 0$ or $|\mathbf{H}(q)\mathbf{g}_b - \mathbf{I} \hbar \omega| = 0$, again come in pairs $\pm \hbar \omega(k)$. The two lower positive bands are given by

$$\begin{aligned} \hbar \omega_{1,2}(k) = 2S & \left\{ (A_x + A_y - 2J_2)(J_1 - J_2) + A_x A_y \right. \\ & - \left[4J_1 J_2^2 (A_x + A_y - 2J_2) + J_2^2 (A_x + A_y - 2J_2)^2 J_1^2 (A_y - A_x)^2 + 2J_1^2 J_2^2 (1 + \cos(kb_m)) \right. \\ & \left. \left. \pm 2 \left(\frac{1}{2} J_1^2 J_2^2 (A_x - A_y)^2 (A_x + A_y + 2J_1 - 2J_2)^2 (1 + \cos(kb_m)) \right)^{1/2} \right]^{1/2} \right\} \end{aligned} \quad (27)$$

where the plus sign corresponds to band 1 and the minus sign to band 2. The two upper positive bands are given by

$$\begin{aligned} \hbar \omega_{3,4}(k) = 2S & \left\{ (A_x + A_y - 2J_2)(J_1 - J_2) + A_x A_y \right. \\ & + \left[4J_1 J_2^2 (A_x + A_y - 2J_2) + J_2^2 (A_x + A_y - 2J_2)^2 J_1^2 (A_y - A_x)^2 + 2J_1^2 J_2^2 (1 + \cos(kb_m)) \right. \\ & \left. \mp 2 \left(\frac{1}{2} J_1^2 J_2^2 (A_x - A_y)^2 (A_x + A_y + 2J_1 - 2J_2)^2 (1 + \cos(kb_m)) \right)^{1/2} \right]^{1/2} \right\} \end{aligned} \quad (28)$$

where the minus sign corresponds to band 3 and the plus sign to band 4. Using parameters corresponding to a hole doping of 0.4 per bulk unit cell (4 Mo atoms and 12 I atoms), $J_1 = 25.42$ meV, $J_2 = -4.26$ meV, $A_y = 2.9$ meV, and $A_x = 0.91$ meV, the positive valued bands are shown in Fig. 5.

The spectrum is now gapped, and the question is whether this gap is a trivial gap or a topological gap. The first indication that there is a topologically non-trivial phase is that when we continually reduce the magnitude of J_2 , the gap in the spectrum closes and re-opens at Γ as shown in Fig. 6. From the analytical expressions (27) and (28) evaluated at $k = 0$, the energies of the 4 bands at Γ are

$$\begin{aligned} E_1 &= 2S \sqrt{A_x(A_y + 2J_1)} \\ E_2 &= 2S \sqrt{A_y(A_x + 2J_1)} \\ E_3 &= 2S \sqrt{(A_x + 2|J_2|)[A_y + 2(J_1 + |J_2|)]} \\ E_4 &= 2S \sqrt{(A_y + 2|J_2|)[A_x + 2(J_1 + |J_2|)]}. \end{aligned} \quad (29)$$

Note that E_2 is independent of J_2 . As $|J_2|$ is reduced, $E_3 = E_2$ when J_2 reaches a critical value J_{2c} given by a quadratic equation, which, when expanded out to first

order in the small parameter $\frac{(A_y - A_x)}{J_1(1 + (A_y + A_x)/(2J_1))^2}$, gives

$$J_{2c} \approx -J_1 \frac{A_y - A_x}{2J_1 + A_x + A_y} \approx -\frac{A_y - A_x}{2} + \frac{A_y^2 - A_x^2}{4J_1}. \quad (30)$$

It is clear from Eq. (30) that both anisotropy and dimerization are required for a band crossing to occur. For the values of J_1 , A_y , and A_x listed in Fig. 5, corresponding to -0.4 filling in Table I, the exact value for J_{2c} is -0.896 meV and the value for J_{2c} from the linearized expression is -0.926 meV. The question is now, what is the nature of the bands on either side of the critical value J_{2c} ? On which side is the gap topological and on which side is it trivial?

To answer this question, we consider the ‘surface Green’s functions’ and the corresponding ‘surface spectral functions’ for the 4 values of J_2 used in Figs. 5 and 6. To obtain the surface Green function, we inverse Fourier transform $\mathbf{H}' \equiv \mathbf{H}(q)\mathbf{g}_b$ back to the lattice representation

$$\mathbf{t}^\dagger \mathbf{U}_{n-1} + (\mathbf{D} - \frac{E}{2} \mathbf{I}) \mathbf{U}_n + \mathbf{t} \mathbf{U}_{n+1} = 0 \quad (31)$$

where \mathbf{U} is now a column of the transformation matrix

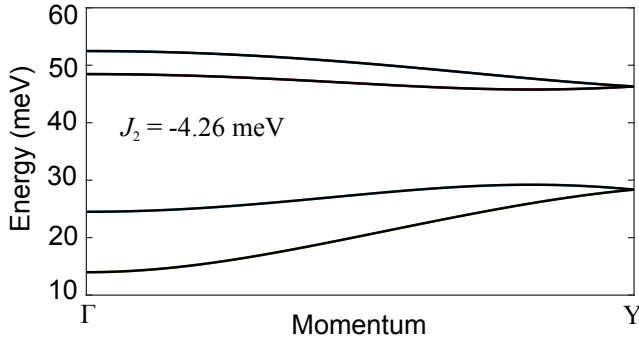


FIG. 5. Magnon spectrum for the magnetic tetramerized 1D chain shown in Fig. 3(b) calculated from Eqs. (27) and (28) with parameters from Table I for 0.4 hole filling: $J_1 = 25.42$ meV, $J_2 = -4.26$ meV, $A_y = 2.9$ meV, and $A_x = 0.91$ meV. Y corresponds to the Brillouin zone edge of the magnetic unit cell, $Y = \frac{\pi}{b_m} = \frac{\pi}{2b}$, where b_m is the magnetic unit cell lattice constant shown in Fig. 3(b).

that diagonalizes \mathbf{H}' [34]. The matrices \mathbf{D} and \mathbf{t} are

$$\mathbf{D} = \begin{bmatrix} \Sigma & \Delta_A & 0 & -J_1 & 0 & 0 & 0 & 0 \\ -\Delta_A & -\Sigma & J_1 & 0 & 0 & 0 & 0 & 0 \\ 0 & -J_1 & \Sigma & \Delta_A & -|J_2| & 0 & 0 & 0 \\ J_1 & 0 & -\Delta_A & -\Sigma & 0 & |J_2| & 0 & 0 \\ 0 & 0 & -|J_2| & 0 & \Sigma & \Delta_A & 0 & -J_1 \\ 0 & 0 & 0 & |J_2| & -\Delta_A & -\Sigma & J_1 & 0 \\ 0 & 0 & 0 & 0 & 0 & -J_1 & \Sigma & \Delta_A \\ 0 & 0 & 0 & 0 & J_1 & 0 & -\Delta_A & -\Sigma \end{bmatrix} \quad (32)$$

and

$$\mathbf{t} = \begin{bmatrix} 0 & 0 & 0 & 0 & 0 & 0 & 0 & 0 \\ 0 & 0 & 0 & 0 & 0 & 0 & 0 & 0 \\ 0 & 0 & 0 & 0 & 0 & 0 & 0 & 0 \\ 0 & 0 & 0 & 0 & 0 & 0 & 0 & 0 \\ 0 & 0 & 0 & 0 & 0 & 0 & 0 & 0 \\ 0 & 0 & 0 & 0 & 0 & 0 & 0 & 0 \\ 0 & 0 & 0 & 0 & 0 & 0 & 0 & 0 \\ -|J_2| & 0 & 0 & 0 & 0 & 0 & 0 & 0 \\ 0 & |J_2| & 0 & 0 & 0 & 0 & 0 & 0 \end{bmatrix}, \quad (33)$$

and \mathbf{I} is the 8×8 identity matrix. With these definitions of \mathbf{D} and \mathbf{t} , we calculate the surface Green's function (G^s) of the semi-infinite chain terminated on the left with atom A using the decimation algorithm [30–32] described in Appendix C. The surface spectral functions, given by $A_s = -2\text{Im}(G_{1,1}^s)$, calculated for the same parameters used in the $E - k$ plots of Figs. 5 and 6 are shown in Fig. 7. The surface state appears for $J_2 > J_{2c}$ and disappears for $J_2 < J_{2c}$. Thus, based on the bulk-boundary correspondence, the magnon spectrum is in a topologically non-trivial state for $J_2 > J_{2c}$.

Since this is a 1D chain, it is tempting to view it as a variant of the SSH model, however, this system is qualitatively different. In the original electronic version of the SSH model [5], bandgap closing occurs at X (the zone boundary) when the tight-binding hopping matrix elements within the unit cell (t_1) and between unit cells

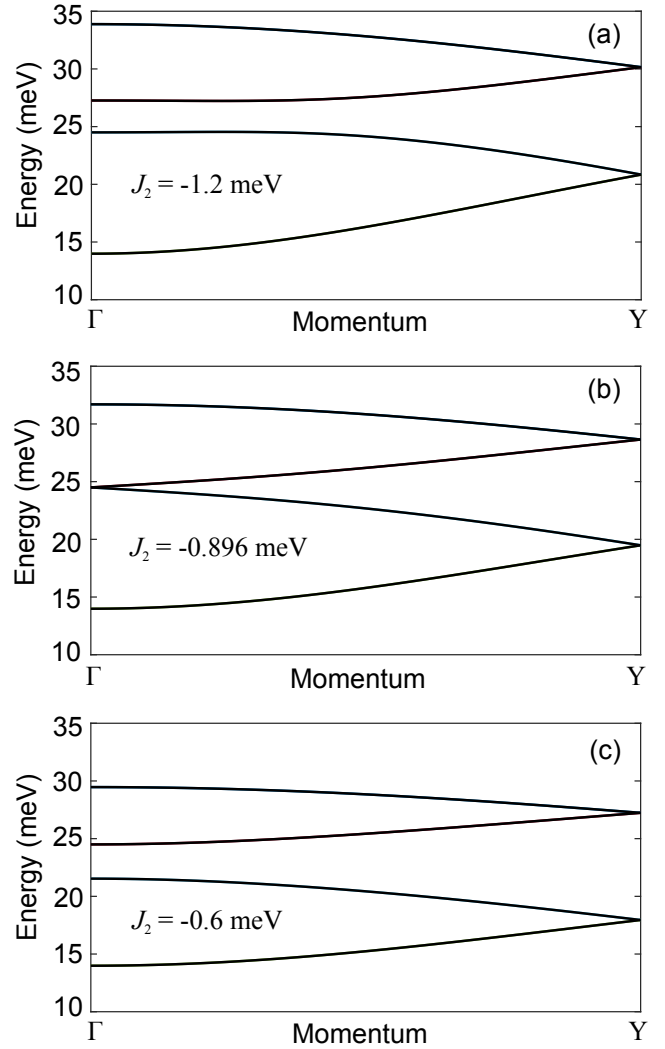


FIG. 6. Magnon spectra as J_2 is changed from (a) -1.2 meV to (b) -0.896 meV to (c) -0.6 meV. The values for J_1 , A_y , and A_x remain the same as in Fig. 5.

(t_2) are equal, i.e. $t_1 = t_2$. Furthermore, the topology is trivial for $|t_1| > |t_2|$ and non-trivial, with a Zak phase equal to 1, when $|t_1| < |t_2|$. Finally, the existence of a surface state in the middle of the bulk gap follows the Shockley criterion, in which a surface state exists when the bond of larger magnitude is cut [37]. Dimerized FM chains, also follow this model. In a dimerized FM chain with alternating values for the nearest neighbor exchange couplings, the magnon gap closes at X when the two exchange constants are equal [7]. In a dimerized chain of FM spheres with nearest-neighbor dipolar coupling, the magnon gap also closes at X when the dipolar coupling within and between unit cells is equal [6]. For both of the above systems, a surface state exists when the linkage corresponding to the stronger coupling is cut. Our 1D chain is doubly dimerized, i.e. there are 4 atoms per magnetic unit cell. Thus, trivial zone-folding occurs such that the Y-point is folded back to Γ and the gap now closes

at Γ . What is qualitatively different about our system is that the magnon gap does not close when $|J_2| = J_1$, but when $|J_2| \approx A_y/2$ (the easy plane anisotropy). For large J_1 , Eq. (30) shows that the critical value for J_2 has negligible dependence on J_1 . Finally, the surface state in the gap exists when we cut the *weaker* coupling J_2 rather than the stronger coupling J_1 . Thus, the physics governing the topological properties this 1D magnonic system are qualitatively different from the physics of the SSH model.

IV. INTERCHAIN COUPLING

A. AFM Charge Neutral Bulk Structure

In the bulk, the chains are arranged in a triangular lattice in the $a-c$ plane as shown in Fig. 1(c,d). The AFM interchain couplings (J_3 and J_4) combined with the triangular lattice give rise to spin frustration, and the lowest energy ground-state spin texture that we have found for the charge neutral bulk structure, both from DFT total energy calculations and from the spin Hamiltonian, is a helical texture, shown in Fig. 1(c,d), such that the interchain, nearest-neighbor spins are rotated by 120° with respect to each other. A further indication that this state is a stable energy minimum is that the magnon dispersion calculations using this state as the ground state give no negative modes. This is similar to the criterion used to determine a stable crystal structure by calculating the phonon dispersion and finding no negative modes. If, for example, we attempt to calculate the magnon dispersion of the charge neutral structure starting from a collinear state, we observe many negative modes.

The bulk magnon dispersion of the charge neutral structure is shown in Fig. 8(a). Even though the interchain exchange couplings (J_3 and J_4) are relatively small compared to J_1 and J_2 , each chain is coupled to 6 neighbors, which significantly enhances their effect. The AFM interchain coupling causes splitting of the single-chain dispersion along the chain direction ($\Gamma - Y$), and it gives rise to cross-chain dispersion ($\Gamma - X$ and $\Gamma - Z$). The energies of the first two excited states at Γ of 18.4 meV and 23.0 meV straddle the energy of the first excited state of the isolated chain of 22.0 meV.

B. AFM / FM Bulk Structure

Considering the parameters in Table I and Eq. (30), the topological transition occurs between a hole doping of 0.2 and 0.3 per primitive unit cell (16 atoms), and the structures with 0.3 and 0.4 hole doping are in the topological magnonic state. The magnon dispersions calculated for 0.3 and 0.4 hole filling are shown in Figs. 8(b,c). For the smaller value of $|J_2| = 2.30$ meV, the gap in the dispersion is closed by the splitting resulting from the interchain coupling. For the larger value of $|J_2| = 4.26$ meV,

the gap in the spectrum of the single-chain spectrum is large enough that the gap remains open in the presence of the interchain coupling, and the topological character of the single-chain dispersion can still be observed. A second result of increased hole doping is increased in-plane ($a-c$ plane) anisotropy (A_x). For both 0.3 and 0.4 hole doping, the ground state spin spiral texture of the charge neutral system shown in Fig. 1(c,d) is replaced by the collinear spin texture with all spins aligned along the $\pm c$ axis ($\pm z$). This minimizes the anisotropy energy from the last term in the Hamiltonian in Eq. (21).

V. CONCLUSIONS

Alternating AFM (J_1) and FM (J_2) exchange couplings along a spin chain can give rise to 1D topological magnon bands depending on the relative magnitudes of J_1 , J_2 , and the anisotropy constants. The topological phase is qualitatively different from that of the SSH model. The existence of such a phase requires dimerization ($|J_2| \neq |J_1|$), alternating AFM and FM coupling ($J_1 > 0$, $J_2 < 0$), and easy-plane anisotropy. The condition for the topological phase with large J_1 is $|J_2| \gtrsim A_y/2$. This is a qualitatively different condition than found in the SSH model. Furthermore, the surface state exists when the weaker bond corresponding to the weaker coupling (J_2) is cut. This condition also contradicts the SSH model. This model system may be physically embodied in MoI_3 . In bulk MoI_3 , the small AFM coupling between the chains, when multiplied by the 6 nearest neighbor chains, becomes significant. Both the sign and magnitude of the intrachain exchange coupling along the longer bond (J_2) are affected by hole filling. The in-plane anisotropy is also affected by hole filling. At larger values of hole filling, the single-chain, topological magnonic gap remains larger than the band splitting resulting from the cross-chain coupling. As a result, MoI_3 may provide a material platform in which multiple magnetic phases, both normal and topological, can be obtained by gating or doping.

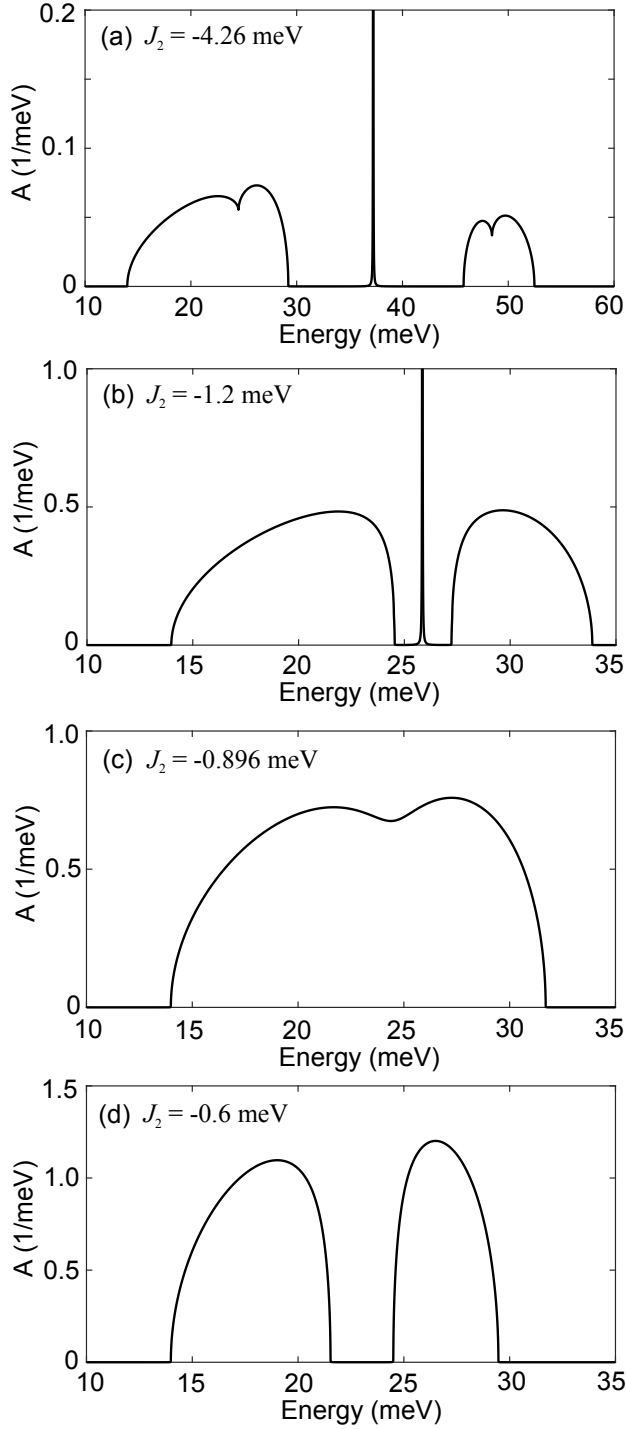


FIG. 7. (a-d) Surface spectral functions calculated for the values of J_2 shown in the plots. These values correspond to those used in the $E - k$ plots shown in Figs. 5 and 6. The values for J_1 , A_y , and A_x remain the same as in Fig. 5. In (a) and (b), the y -axis has been truncated, so that the band contributions to A are visible. The height of the peaks of the surface states are on the order of 10^3 (1/meV).

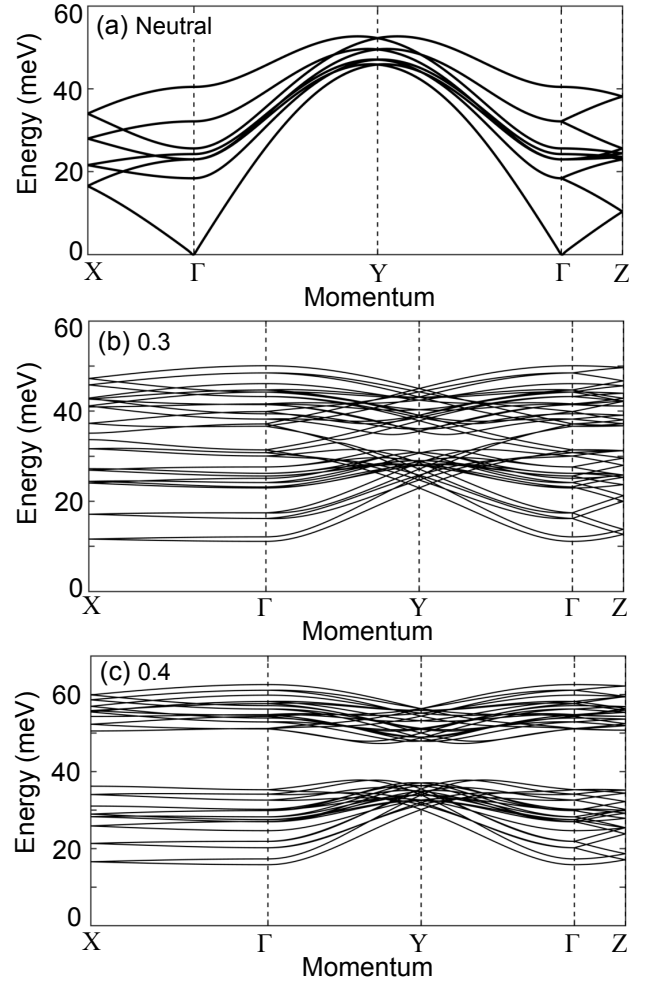


FIG. 8. Bulk magnon dispersions calculated for (a) neutral, (b) 0.3, and (c) 0.4 hole filling. All values are taken from the Table I.

ACKNOWLEDGMENTS

This work was supported by the Vannevar Bush Faculty Fellowship from the Office of Secretary of Defense (OSD) under the Office of Naval Research (ONR) contract N00014-21-1-2947 on One-Dimensional Quantum Materials. DFT calculations were performed on STAMPEDE2 at TACC and EXPANSE at SDSC under allocation DMR130081 from the Advanced Cyberinfrastructure Coordination Ecosystem: Services & Support (ACCESS) program [38], which is supported by National Science Foundation grants #2138259, #2138286, #2138307, #2137603, and #2138296. R. Lake acknowledges useful discussions with Ran Cheng and Hantao Zhang.

Appendix A: Exchange constants

To calculate the exchange constants, we use the energy mapping method [10, 27–29]. In this method, we calculate the total energy for different FM and AFM configurations of MoI_3 using PBE-D3 with spin-orbit coupling (SOC) and equate this energy with the energy resulting from the Hamiltonians in Eqs. (1) or (21). Since there are 4 exchange constants ($J_1 \dots J_4$) and an unknown energy E_0 resulting from the non-magnetic components of the total energy functional in the DFT calculations, we consider five different spin configurations (1 FM and 4 AFM states), as illustrated in Fig. 9. All spins are aligned along the $\pm c$ axis. In all of these configurations, the unit cell is doubled along the chain direction. As shown in figure 9(a), the exchange constants J_1 and J_2 represent the intrachain short and long Mo-Mo coupling, and J_3 and J_4 are the interchain exchange couplings. The primary through-bond paths mediating J_3 and J_4 are illustrated in Fig. 9(a). The total energy of these five configurations can be derived from the magnetic Hamiltonian as:

$$\begin{aligned}
 E_{FM} &= E_0 + 8J_1 + 8J_2 + 48J_3 + 96J_4 \\
 E_{AFM1} &= E_0 - 8J_1 - 8J_2 + 48J_3 - 96J_4 \\
 E_{AFM2} &= E_0 - 8J_1 - 8J_2 - 16J_3 + 32J_4 \\
 E_{AFM3} &= E_0 - 8J_1 + 8J_2 + 16J_3 + 0J_4 \\
 E_{AFM4} &= E_0 + 8J_1 + 8J_2 - 16J_3 - 32J_4
 \end{aligned} \tag{A1}$$

To determine the anisotropy energies, the spin configuration of Fig. 9(d) is used. Three total energy calculations are performed with all spins aligned along $\pm x$, $\pm y$, and $\pm z$, and the energy differences give the anisotropy energies per Mo atom, $A_x = (E_x - E_z)/8$ and $A_y = (E_y - E_z)/8$, where E_ν is the total energy of the supercell with the spins aligned along the $\pm\nu$ directions.

The above energy mapping approach, while heavily used throughout the literature, can be viewed as the lowest level of theory for constructing a spin Hamiltonian that maps the total energies calculated from DFT. At the next level of sophistication, the exchange constants can be replaced by exchange tensors as described in [39, 40].

The tensors representing J_1 and J_2 in MoI_3 each have three independent symmetry allowed diagonal elements. The symmetry allowed full symmetric tensors representing J_3 and J_4 each have 6 independent elements. Thus, the symmetry allowed exchange tensors representing J_1 - J_4 contain 18 exchange parameters. Using the four-state energy mapping method [39] would require a $3 \times 3 \times 3$ supercell, consisting of 432 atoms, and 4 total energy calculations for each of the 18 exchange parameters. The number of parameters can be reduced by using analytical expressions for the exchange constants and assuming symmetries to reduce the number of free parameters, such as in-plane isotropy [40]. Determining the full tensors would require a more sophisticated approach such as the Green's function or Liechtenstein approach [41–43]. These latter approaches can provide greater physical insight into the exchange couplings resulting from different orbitals, however, when using a plane-wave DFT code, they require a transformation into the Wannier basis, which can be problematic for larger unit cells.

Under hole doping, the presence of itinerant holes raises questions about the validity of the Heisenberg type Hamiltonians, which assume localized spins, relatively localized exchange interactions, and absence of longitudinal spin modes (i.e. uniform magnitude of magnetic moments). Electronic structure calculations described in App. B show that the partially occupied frontier d-orbital valence band is very narrow indicating strong localization of the holes residing on the Mo atoms. Furthermore the self-consistent field DFT calculations of the supercells find that the magnitudes of the Mo magnetic moments to be identical. Thus, the use of the Heisenberg type Hamiltonians can be justified.

Appendix B: Electronic bands

To see the effect of hole filling on the Fermi level, we have calculated the electronic bands of MoI_3 with SOC. Figure 10 shows the electronic bands of the AFM state of MoI_3 with different hole fillings. Neutral MoI_3 is a semiconductor with a calculated bandgap of 1.094 eV (which is close to the experimental value of 1.27 eV [9]). The uppermost 4 valence bands are narrow bands composed of the d-orbitals of the Mo atoms. Hole doping causes the uppermost valence band to become partially unoccupied. The narrow bandwidth of the uppermost valence band indicates strong localization of the frontier d-orbital band and thus strong localization of the itinerant holes.

Appendix C: Decimation Algorithm

Using matrices (32) and (33), we implement the decimation algorithm [30–32] for calculating the surface Green function. For calculating the surface Green function of the semi-infinite slab terminated on the left with

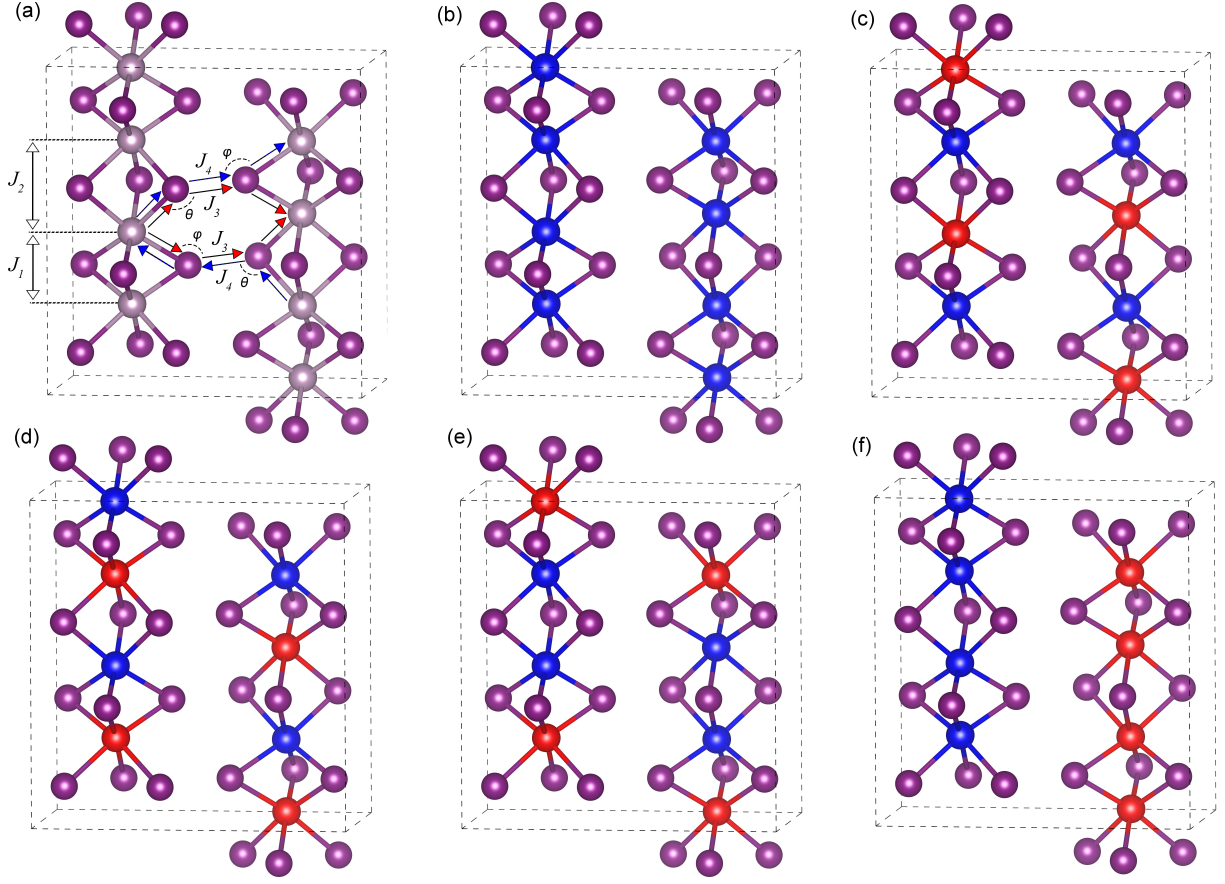


FIG. 9. (a) Illustration of the 4 exchange constants. The shortest through-bond paths are shown for J_3 (in red) and J_4 (in blue). The bond angles for the upper and lower paths for J_4 are shown. The angles are $\theta = 91.6^\circ$ and $\varphi = 139.2^\circ$. The lower path is the reverse of the upper path. (b-f) Different spin configurations used for the total energy calculations. Red and blue atoms represent opposite spins.

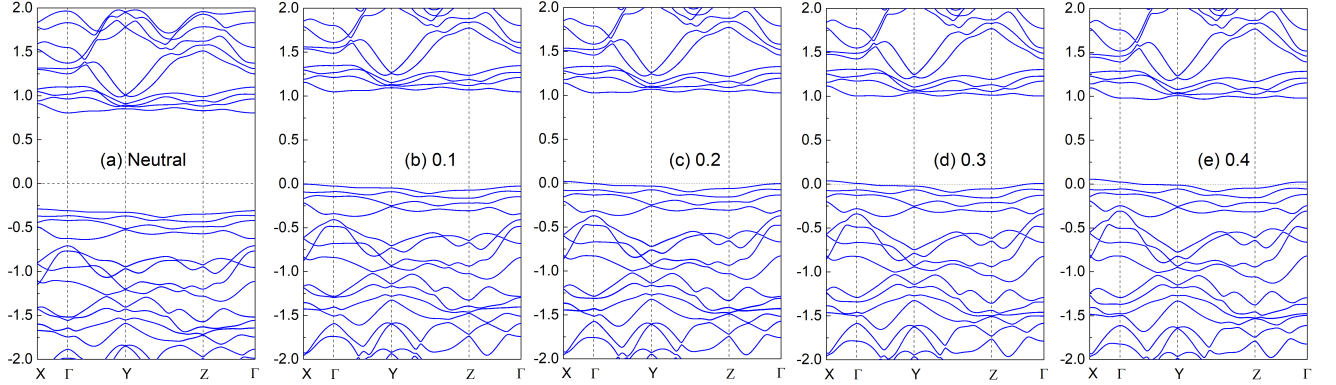


FIG. 10. Electronic band diagrams of MoI_3 for different hole fillings as labeled in the plots.

atom A , we define the following

$$\begin{aligned}
 \mathbf{D}_0^s &= \mathbf{D} \\
 \mathbf{D}_0 &= \mathbf{D} \\
 \mathbf{A}_0 &= \mathbf{t} \\
 \mathbf{B}_0 &= \mathbf{t}^\dagger,
 \end{aligned} \tag{C1}$$

where the subscript now indicates the iteration number. We now iterate

$$\begin{aligned}
 \mathbf{D}_i^s &= \mathbf{D}_{i-1}^s + \mathbf{A}_{i-1} [(E + i\eta)\mathbf{I} - \mathbf{D}_{i-1}]^{-1} \mathbf{B}_{i-1} \\
 \mathbf{D}_i &= \mathbf{D}_{i-1} + \mathbf{A}_{i-1} [(E + i\eta)\mathbf{I} - \mathbf{D}_{i-1}]^{-1} \mathbf{B}_{i-1} \\
 &\quad + \mathbf{B}_{i-1} [(E + i\eta)\mathbf{I} - \mathbf{D}_{i-1}]^{-1} \mathbf{A}_{i-1} \\
 \mathbf{A}_i &= \mathbf{A}_{i-1} [(E + i\eta)\mathbf{I} - \mathbf{D}_{i-1}] \mathbf{A}_{i-1} \\
 \mathbf{B}_i &= \mathbf{B}_{i-1} [(E + i\eta)\mathbf{I} - \mathbf{D}_{i-1}] \mathbf{B}_{i-1}
 \end{aligned} \tag{C2}$$

until the original 2×2 non-zero coupling blocks of \mathbf{A}_i are negligible. In practice, once all elements of \mathbf{A}_i are less than 1.0×10^{-9} meV, we exit the iteration loop. The 8×8 surface Green function is then

$$\mathbf{G}^s = (E\mathbf{I} - \mathbf{D}_i^s)^{-1}. \quad (\text{C3})$$

The value of η used was 1.0×10^{-3} meV.

Appendix D: Effective Field Calculation of Magnon Dispersion

In this appendix, we describe the classical, effective field approach for calculating the magnon dispersions for the single-chain structures illustrated in Fig. 3.

1. Dimerized Chain with $J_1, J_2 > 0$

We first consider the structure of Fig. 3(a) with the Hamiltonian given in Eq. (1). From the Hamiltonian, we identify the effective field acting on the the spins. The magnetic moment associated with each spin A or B in the unit cell is

$$m_n^{A,B} = -g\mu_B \mathbf{S}_n^{A,B} \quad (\text{D1})$$

The effective field acting on magnetic moment m_n^α is given by $-\partial H/\partial m_n^\alpha$. The effective fields are

$$\mathbf{B}_{\text{eff},n}^A = \frac{2}{g\mu_B} (J_1 \mathbf{S}_n^B + J_2 \mathbf{S}_{n-1}^B) + \frac{2A_y}{g\mu_B} S_{n,y}^A \hat{y} + \frac{2A_x}{g\mu_B} S_{n,x}^A \hat{x},$$

and

$$\mathbf{B}_{\text{eff},n}^B = \frac{2}{g\mu_B} (J_1 \mathbf{S}_n^A + J_2 \mathbf{S}_{n+1}^A) + \frac{2A_y}{g\mu_B} S_{n,y}^B \hat{y} + \frac{2A_x}{g\mu_B} S_{n,x}^B \hat{x}.$$

The equations of motions for the angular momenta defined by the spins are

$$\hbar \frac{d\mathbf{S}_n^A}{dt} = \boldsymbol{\mu}_n^A \times \mathbf{B}_{\text{eff},n}^A \quad (\text{D2})$$

or

$$\hbar \frac{d\mathbf{S}_n^A}{dt} = -g\mu_B \mathbf{S}_n^A \times \mathbf{B}_{\text{eff},n}^A, \quad (\text{D3})$$

and similarly,

$$\hbar \frac{d\mathbf{S}_n^B}{dt} = -g\mu_B \mathbf{S}_n^B \times \mathbf{B}_{\text{eff},n}^B. \quad (\text{D4})$$

Writing out (D3) and (D4) gives

$$\begin{aligned} \hbar \dot{\mathbf{S}}_n^A &= -\mathbf{S}_n^A \times 2 [J_1 \mathbf{S}_n^B + J_2 \mathbf{S}_{n-1}^B + A_y S_{n,y}^A \hat{y} + A_x S_{n,x}^A \hat{x}] \\ \hbar \dot{\mathbf{S}}_n^B &= -\mathbf{S}_n^B \times 2 [J_1 \mathbf{S}_n^A + J_2 \mathbf{S}_{n+1}^A + A_y S_{n,y}^B \hat{y} + A_x S_{n,x}^B \hat{x}]. \end{aligned}$$

In linear response, we assume the deviations from the equilibrium alignments are small. Therefore, $S_{n,z}^A = S$ and $S_{n,z}^B = -S$. The equations of motion for the x and y components of $\dot{\mathbf{S}}_n^A$ and $\dot{\mathbf{S}}_n^B$ are

$$\begin{aligned} \hbar \dot{S}_{n,x}^A &= 2S [(J_1 + J_2 + A_y) S_{n,y}^A + J_1 S_{n,y}^B + J_2 S_{n-1,y}^B] \\ \hbar \dot{S}_{n,y}^A &= -2S [(J_1 + J_2 + A_x) S_{n,x}^A + J_1 S_{n,x}^B + J_2 S_{n-1,x}^B] \\ \hbar \dot{S}_{n,x}^B &= -2S [(J_1 + J_2 + A_y) S_{n,y}^B + J_1 S_{n,y}^A + J_2 S_{n+1,y}^A] \\ \hbar \dot{S}_{n,y}^B &= 2S [(J_1 + J_2 + A_x) S_{n,x}^B + J_1 S_{n,x}^A + J_2 S_{n+1,x}^A]. \end{aligned} \quad (\text{D5})$$

Assume a plane-wave solution such that

$$\begin{aligned} S_{n,x}^A &= S_x^A e^{i(kbn - \omega t)} \\ S_{n,y}^A &= S_y^A e^{i(kbn - \omega t)} \\ S_{n,x}^B &= S_x^B e^{i(kbn - \omega t)} \\ S_{n,y}^B &= S_y^B e^{i(kbn - \omega t)} \end{aligned} \quad (\text{D6})$$

where the unknown coefficients S_x^A , S_y^A , S_x^B , and S_y^B are complex amplitudes, b is the lattice constant, and n is the unit cell index. Placing these forms of the solutions into Eqs. (D5), we have

$$\begin{aligned} -i\hbar\omega S_x^A &= 2S [(J_1 + J_2 + A_y) S_y^A + (J_1 + J_2 e^{-ika}) S_y^B] \\ -i\hbar\omega S_y^A &= -2S [(J_1 + J_2 + A_x) S_x^A + (J_1 + J_2 e^{-ika}) S_x^B] \\ -i\hbar\omega S_x^B &= -2S [(J_1 + J_2 + A_y) S_y^B + (J_1 + J_2 e^{+ika}) S_y^A] \\ -i\hbar\omega S_y^B &= 2S [(J_1 + J_2 + A_x) S_x^B + (J_1 + J_2 e^{+ika}) S_x^A]. \end{aligned} \quad (\text{D7})$$

Re-writing (D7) as a matrix eigenvalue equation gives

$$\begin{bmatrix} -\hbar\omega & i2S(J_1 + J_2 + A_y) & 0 & i2S(J_1 + J_2 e^{-ika}) \\ -i2S(J_1 + J_2 + A_x) & -\hbar\omega & -i2S(J_1 + J_2 e^{-ika}) & 0 \\ 0 & -i2S(J_1 + J_2 e^{+ika}) & -\hbar\omega & -i2S(J_1 + J_2 + A_y) \\ i2S(J_1 + J_2 e^{+ika}) & 0 & i2S(J_1 + J_2 + A_x) & -\hbar\omega \end{bmatrix} \begin{bmatrix} S_x^A \\ S_y^A \\ S_x^B \\ S_y^B \end{bmatrix} = 0. \quad (\text{D8})$$

Setting the determinant to zero, gives 4 solutions for $\hbar\omega$

of the form $\pm\hbar\omega_0(k)$ and $\pm\hbar\omega_1(k)$. The two positive

solutions are given by Eqs. (11) and (12) of the main text.

2. Tetramerized Chain with $J_1 > 0$ and $J_2 < 0$

We now consider the structure in Fig. 3(b) with Hamiltonian given by Eq. (21). Proceeding as above, the effective fields are

$$\begin{aligned} B_{\text{eff},n}^A &= \frac{2}{g\mu_B} [J_1 S_n^B + J_2 S_{n-1}^D + A_y S_{n,y}^A \hat{y} + A_x S_{n,x}^A \hat{x}] \\ B_{\text{eff},n}^B &= \frac{2}{g\mu_B} [J_1 S_n^A + J_2 S_n^C + A_y S_{n,y}^B \hat{y} + A_x S_{n,x}^B \hat{x}] \\ B_{\text{eff},n}^C &= \frac{2}{g\mu_B} [J_2 S_n^B + J_1 S_n^D + A_y S_{n,y}^C \hat{y} + A_x S_{n,x}^C \hat{x}] \\ B_{\text{eff},n}^D &= \frac{2}{g\mu_B} [J_1 S_n^C + J_2 S_{n+1}^A + A_y S_{n,y}^D \hat{y} + A_x S_{n,x}^D \hat{x}], \end{aligned} \quad (\text{D9})$$

and the resulting equations of motion are

$$\begin{aligned} \hbar \dot{S}_n^A &= -S_n^A \times 2 [J_1 S_n^B + J_2 S_{n-1}^D + A_y S_{n,y}^A \hat{y} + A_x S_{n,x}^A \hat{x}] \\ \hbar \dot{S}_n^B &= -S_n^B \times 2 [J_1 S_n^A + J_2 S_n^C + A_y S_{n,y}^B \hat{y} + A_x S_{n,x}^B \hat{x}] \\ \hbar \dot{S}_n^C &= -S_n^C \times 2 [J_2 S_n^B + J_1 S_n^D + A_y S_{n,y}^C \hat{y} + A_x S_{n,x}^C \hat{x}] \\ \hbar \dot{S}_n^D &= -S_n^D \times 2 [J_1 S_n^C + J_2 S_{n+1}^A + A_y S_{n,y}^D \hat{y} + A_x S_{n,x}^D \hat{x}]. \end{aligned} \quad (\text{D10})$$

Inserting plane wave solutions $S_{n,\alpha}^\alpha = S_{xy}^\alpha e^{i(kan - \omega t)}$ and setting $S_z^A = S_z^D = S$ and $S_z^B = S_z^C = -S$, we have

$$\hbar \omega S_x^A = 2iS [(J_1 - J_2 + A_y)S_y^A + J_1 S_y^B + J_2 S_y^D e^{-ika}]$$

$$\hbar \omega S_y^A = -2iS [(J_1 - J_2 + A_x)S_x^A + J_1 S_x^B + J_2 S_x^D e^{-ika}]$$

$$\hbar \omega S_x^B = -2iS [(J_1 - J_2 + A_y)S_y^B + J_1 S_y^A + J_2 S_y^C]$$

$$\hbar \omega S_y^B = 2iS [(J_1 - J_2 + A_x)S_x^B + J_1 S_x^A + J_2 S_x^C]$$

$$\hbar \omega S_x^C = -2iS [(J_1 - J_2 + A_y)S_y^C + J_2 S_y^B + J_1 S_y^D]$$

$$\hbar \omega S_y^C = 2iS [(J_1 - J_2 + A_x)S_x^C + J_2 S_x^B + J_1 S_x^D]$$

$$\hbar \omega S_x^D = 2iS [(J_1 - J_2 + A_y)S_y^D + J_1 S_y^C + J_2 S_y^A e^{ika}]$$

$$\hbar \omega S_y^D = -2iS [(J_1 - J_2 + A_x)S_x^D + J_1 S_x^C + J_2 S_x^A e^{ika}]$$

Using the following definitions,

$$\begin{aligned} t_x &= 2iS(J_1 - J_2 + A_x) \\ t_y &= 2iS(J_1 - J_2 + A_y) \\ \tilde{J}_1 &= 2iSJ_1 \\ \tilde{J}_2 &= 2iSJ_2, \end{aligned} \quad (\text{D11})$$

the energies $\hbar \omega$ are the eigenenergies of an 8×8 matrix,

$$\begin{bmatrix} -\hbar\omega & t_y & 0 & \tilde{J}_1 & 0 & 0 & 0 & \tilde{J}_2 e^{-ikb_m} \\ -t_x & -\hbar\omega & \tilde{J}_1 & 0 & 0 & 0 & -\tilde{J}_2 e^{-ikb_m} & 0 \\ 0 & -\tilde{J}_1 & -\hbar\omega & -t_y & 0 & -\tilde{J}_2 & 0 & 0 \\ \tilde{J}_1 & 0 & t_x & -\hbar\omega & \tilde{J}_2 & 0 & 0 & 0 \\ 0 & 0 & 0 & -\tilde{J}_2 & -\hbar\omega & -t_y & 0 & -\tilde{J}_1 \\ 0 & 0 & \tilde{J}_2 & 0 & t_x & -\hbar\omega & \tilde{J}_1 & 0 \\ 0 & \tilde{J}_2 e^{ikb_m} & 0 & 0 & 0 & \tilde{J}_1 & -\hbar\omega & t_y \\ -\tilde{J}_2 e^{ikb_m} & 0 & 0 & 0 & -\tilde{J}_1 & 0 & -t_x & -\hbar\omega \end{bmatrix} \begin{bmatrix} S_x^A \\ S_y^A \\ S_x^B \\ S_y^B \\ S_x^C \\ S_y^C \\ S_x^D \\ S_y^D \end{bmatrix} = 0. \quad (\text{D12})$$

Setting the determinant to zero gives 4 pairs of bands $\pm \hbar \omega(k)$. The four positive bands are given by Eqs. (27) and (28) of the main text.

-
- [1] X. S. Wang, H. W. Zhang, and X. R. Wang, Topological magnonics: A paradigm for spin-wave manipulation and device design, *Phys. Rev. Appl.* **9**, 024029 (2018).
[2] Z.-X. Li, Y. Cao, and P. Yan, Topological insulators and semimetals in classical magnetic systems, *Physics Reports* **915**, 1 (2021).
[3] P. A. McClarty, Topological magnons: A review, *Annual*

- Review of Condensed Matter Physics* **13**, 171 (2022).
[4] H. Zhang and R. Cheng, A perspective on magnon spin Nernst effect in antiferromagnets, *Applied Physics Letters* **120**, 090502 (2022).
[5] W. P. Su, J. R. Schrieffer, and A. J. Heeger, Solitons in polyacetylene, *Phys. Rev. Lett.* **42**, 1698 (1979).
[6] F. Pirmoradian, B. Zare Rameshti, M. Miri, and S. Saei-

- dian, Topological magnon modes in a chain of magnetic spheres, *Phys. Rev. B* **98**, 224409 (2018).
- [7] P.-T. Wei, J.-Y. Ni, X.-M. Zheng, D.-Y. Liu, and L.-J. Zou, Topological magnons in one-dimensional ferromagnetic Su-Schrieffer-Heeger model with anisotropic interaction, *Journal of Physics: Condensed Matter* **34**, 495801 (2022).
- [8] M. Ströbele, R. Thalwitzer, and H.-J. Meyer, Facile way of synthesis for molybdenum iodides, *Inorganic Chemistry* **55**, 12074 (2016).
- [9] K. H. Choi, S. Oh, S. Chae, B. J. Jeong, B. J. Kim, J. Jeon, S. H. Lee, S. O. Yoon, C. Woo, X. Dong, A. Ghulam, C. Lim, Z. Liu, C. Wang, A. Junaid, J.-H. Lee, H. K. Yu, and J.-Y. Choi, Low ligand field strength ion (I⁻) mediated 1D inorganic material MoI₃: Synthesis and application to photo-detectors, *Journal of Alloys and Compounds* **853**, 157375 (2021).
- [10] F. Kargar, Z. Barani, N. R. Sesing, T. T. Mai, T. Debnath, H. Zhang, Y. Liu, Y. Zhu, S. Ghosh, A. J. Biccchi, F. H. da Jornada, L. Bartels, T. Adel, A. R. Hight Walker, A. V. Davydov, T. T. Salguero, R. K. Lake, and A. A. Balandin, Elemental excitations in MoI₃ one-dimensional van der waals nanowires, *Applied Physics Letters* **121**, 221901 (2022).
- [11] L. Fu, C. Shang, S. Zhou, Y. Guo, and J. Zhao, Transition metal halide nanowires: A family of one-dimensional multifunctional building blocks, *Applied Physics Letters* **120**, 023103 (2022).
- [12] A. Mella, E. Suárez-Morell, and A. S. Nunez, Magnetic spirals and biquadratic exchange in 1D MoX₃ spin chains, *Journal of Magnetism and Magnetic Materials* **594**, 171882 (2024).
- [13] K. Momma and F. Izumi, *VESTA3* for three-dimensional visualization of crystal, volumetric and morphology data, *Journal of Applied Crystallography* **44**, 1272 (2011).
- [14] S. Toth and B. Lake, Linear spin wave theory for single-Q incommensurate magnetic structures, *Journal of Physics: Condensed Matter* **27**, 166002 (2015).
- [15] K. Yosida, *Theory of Magnetism* (Springer-Verlag, New York, 1991).
- [16] W. Nolting and A. Ramakanth, *Quantum Theory of Magnetism* (Springer, New York, 2009).
- [17] S. M. Rezende, *Lecture Notes in Physics - Fundamentals of Magnonics*, Vol. 969 (Springer Nature Switzerland AG, Cham, 2020).
- [18] G. Kresse and J. Hafner, Ab initio molecular dynamics for liquid metals, *Phys. Rev. B* **47**, 558 (1993).
- [19] G. Kresse and J. Hafner, Ab initio molecular-dynamics simulation of the liquid-metal-amorphous-semiconductor transition in germanium, *Phys. Rev. B* **49**, 14251 (1994).
- [20] G. Kresse and J. Furthmüller, Efficient iterative schemes for ab initio total-energy calculations using a plane-wave basis set, *Phys. Rev. B* **54**, 11169 (1996).
- [21] G. Kresse and J. Furthmüller, Efficiency of ab-initio total energy calculations for metals and semiconductors using a plane-wave basis set, *Comput. Mater. Sci.* **6**, 15 (1996).
- [22] J. P. Perdew, K. Burke, and M. Ernzerhof, Generalized gradient approximation made simple, *Phys. Rev. Lett.* **77**, 3865 (1996).
- [23] S. Grimme, J. Antony, S. Ehrlich, and H. Krieg, A consistent and accurate ab initio parametrization of density functional dispersion correction (DFT-D) for the 94 elements H-Pu, *The Journal of Chemical Physics* **132**, 154104 (2010).
- [24] A. Togo, L. Chaput, T. Tadano, and I. Tanaka, Implementation strategies in phonopy and phono3py, *J. Phys. Condens. Matter* **35**, 353001 (2023).
- [25] A. Togo, First-principles phonon calculations with phonopy and phono3py, *J. Phys. Soc. Jpn.* **92**, 012001 (2023).
- [26] C. E. Calderon, J. J. Plata, C. Toher, C. Oses, O. Levy, M. Fornari, A. Natan, M. J. Mehl, G. Hart, M. Buongiorno Nardelli, and S. Curtarolo, The AFLOW standard for high-throughput materials science calculations, *Computational Materials Science* **108**, 233 (2015).
- [27] J. Kang, C. Lee, R. K. Kremer, and M.-H. Whangbo, Consequences of the intrachain dimer-monomer spin frustration and the interchain dimer-monomer spin exchange in the diamond-chain compound azurite Cu₃(CO₃)₂(OH)₂, *Journal of Physics: Condensed Matter* **21**, 392201 (2009).
- [28] L.-F. Lin, R. Soni, Y. Zhang, S. Gao, A. Moreo, G. Alvarez, A. D. Christianson, M. B. Stone, and E. Dagotto, Electronic structure, magnetic properties, and pairing tendencies of the copper-based honeycomb lattice Na₂Cu₂TeO₆, *Phys. Rev. B* **105**, 245113 (2022).
- [29] Y. Liu, S. Kwon, G. J. de Coster, R. K. Lake, and M. R. Neupane, Structural, electronic, and magnetic properties of CrTe₂, *Phys. Rev. Mater.* **6**, 084004 (2022).
- [30] M. P. L. Sancho, J. M. L. Sancho, and J. Rubio, Quick iterative scheme for the calculation of transfer matrices: application to Mo (100), *Journal of Physics F: Metal Physics* **14**, 1205 (1984).
- [31] M. P. L. Sancho, J. M. L. Sancho, and J. Rubio, Highly convergent schemes for the calculation of bulk and surface Green functions, *J. Phys. F* **15**, 851 (1985).
- [32] M. Galperin, S. Toledo, and A. Nitzan, Numerical computation of tunneling fluxes, *J. Chem. Phys.* **117**, 10817 (2002).
- [33] T. Holstein and H. Primakoff, Field dependence of the intrinsic domain magnetization of a ferromagnet, *Phys. Rev.* **58**, 1098 (1940).
- [34] R. M. White, M. Sparks, and I. Ortenburger, Diagonalization of the antiferromagnetic magnon-phonon interaction, *Phys. Rev.* **139**, A450 (1965).
- [35] J. H. P. Colpa, Diagonalization of the quadratic boson Hamiltonian, *Physica A: Statistical Mechanics and its Applications* **93**, 327 (1978).
- [36] C. Kittel, *Introduction to Solid State Physics*, 7th ed. (John Wiley & Sons, New York, 1996).
- [37] W. Shockley, On the surface states associated with a periodic potential, *Physical Review* **56**, 317 (1939).
- [38] T. J. Boerner, S. Deems, T. R. Furlani, S. L. Knuth, and J. Towns, Access: Advancing innovation: Nsf's advanced cyberinfrastructure coordination ecosystem: Services & support, in *Practice and Experience in Advanced Research Computing*, PEARC '23 (Association for Computing Machinery, New York, NY, USA, 2023) pp. 173–176.
- [39] D. Šabani, C. Bacaksiz, and M. V. Milošević, Ab initio methodology for magnetic exchange parameters: Generic four-state energy mapping onto a Heisenberg spin hamiltonian, *Phys. Rev. B* **102**, 014457 (2020).
- [40] S. Tiwari, M. L. Van de Put, B. Sorée, and W. G. Vandenberghe, Critical behavior of the ferromagnets CrI₃, CrBr₃, and CrGeTe₃ and the antiferromagnet FeCl₂: A detailed first-principles study, *Phys. Rev. B* **103**, 014432 (2021).

- [41] D. M. Korotin, V. V. Mazurenko, V. I. Anisimov, and S. V. Streltsov, Calculation of exchange constants of the heisenberg model in plane-wave-based methods using the Green's function approach, *Phys. Rev. B* **91**, 224405 (2015).
- [42] A. Terasawa, M. Matsumoto, T. Ozaki, and Y. Gohda, Efficient algorithm based on Liechtenstein method for computing exchange coupling constants using localized basis set, *Journal of the Physical Society of Japan* **88**, 114706 (2019).
- [43] X. He, N. Helbig, M. J. Verstraete, and E. Bousquet, TB2J: A python package for computing magnetic interaction parameters, *Computer Physics Communications* **264**, 107938 (2021).